




Design and preparation of ternary α -Fe₂O₃/SnO₂/rGO nanocomposite as an electrode material for supercapacitor

M. Geerthana¹, S. Prabhu¹, S. Harish^{2,3}, M. Navaneethan⁴, R. Ramesh^{1,*} , and M. Selvaraj^{5,*}

¹Department of Physics, Periyar University, Salem, Tamil Nadu 636011, India

²Research Institute of Electronics, Shizuoka University, 3-5-1 Johoku, Naka-ku, Hamamatsu, Shizuoka 432-8011, Japan

³Department of Physics and Nanotechnology, Center for Materials Science and Nano Devices, SRM Institute of Science and Technology, Kattankulathur, Kanchipuram, Tamil Nadu 603203, India

⁴Nanotechnology Research Centre (NRC), SRM Institute of Science and Technology, Kattankulathur, Kanchipuram, Tamil Nadu 603203, India

⁵Department of Chemistry, Faculty of Science, King Khalid University, Abha 61413, Saudi Arabia

Received: 28 January 2021

Accepted: 4 May 2021

Published online:

18 May 2021

© The Author(s), under exclusive licence to Springer Science+Business Media, LLC, part of Springer Nature 2021

ABSTRACT

The development of efficient, scalable, and economically viable electrode materials with high specific capacitance is of great significance for supercapacitor applications. Herein, α -Fe₂O₃ nanoparticles, α -Fe₂O₃/rGO, and α -Fe₂O₃/SnO₂/rGO nanocomposite were synthesized by a one-step hydrothermal method. Different characterization techniques were used to study the physical and chemical properties of the prepared materials. The powder XRD measurement revealed that the formation of the ternary composite without any impurities. As characterized by SEM and TEM techniques, both α -Fe₂O₃ and SnO₂ nanoparticles were embedded on two-dimensional reduced graphene oxide sheets. The electrochemical properties of the prepared electrode materials were studied by cyclic voltammetry and galvanostatic charge/discharge, and impedance spectroscopy techniques in a 6 M KOH electrolyte solution. All the electrode materials exhibit Faradic reaction peaks in CV curves which imply the pseudocapacitive nature of the prepared materials. The ternary α -Fe₂O₃/SnO₂/rGO nanocomposite demonstrated the enhanced specific capacitance of 821 Fg⁻¹ at 1Ag⁻¹ than that of α -Fe₂O₃ nanoparticles (373 Fg⁻¹ at 1Ag⁻¹), and α -Fe₂O₃/rGO (517 Fg⁻¹ at 1Ag⁻¹) nanocomposite with excellent cyclic retention (98.7%) after successive 10,000 cycles. This improved electrochemical performance of ternary α -Fe₂O₃/SnO₂/rGO nanocomposite is mainly attributed to the surface properties of nanostructures of metal oxides and an excellent conductive network. Moreover, the asymmetric supercapacitor (ASC) device was fabricated using the ternary α -Fe₂O₃/SnO₂/rGO nanocomposite as the anode material and

Address correspondence to E-mail: rameshphys@gmail.com; rameshphys@periyaruniversity.ac.in; mselvaraj@kku.edu.sa

rGO as the cathode material. The ASC device showed an energy density of 17 Wh Kg⁻¹ at a power density of 3585 W kg⁻¹ and retains 94.52% capacitance after successive 5000 cycles at a current density of 10Ag⁻¹.

1 Introduction

The fast charge and discharge rates, high power density, and longer life cycle of supercapacitors (SCs) make them a vital device in an emerging energy storage field [1]. The SCs can be classified into two categories based on their charge storage mechanism namely electric double-layer capacitor (EDLCs) and pseudocapacitors [2]. In the EDLCs, the energy storage mechanism is mainly based on the adsorption of ions at the interface between electrode and electrolyte. In the case of pseudocapacitors, the charge storage mechanism involves fast Faradaic reactions [3]. However, the charge/discharge rates of pseudocapacitors were hindered by their rates of Faradic reactions. The performance of SCs is strongly determined by the inherent characteristics of the electrode materials [4, 5]. Transition metal oxides such as RuO₂ [6], Fe₂O₃ [7], SnO₂ [8], CO₃O₄ [9], NiO [10], and MnO₂ [11] have been used as pseudocapacitive materials due to their superior electrochemical properties. Among them, α -Fe₂O₃ is a potential material and has been drawn much attention due to its high theoretical capacitance (974 mAh g⁻¹), low cost, natural abundance, and environmental friendliness [12]. However, the poor electrical conductivity and insufficient ionic diffusion rates of the α -Fe₂O₃ electrode extend the low specific capacitances, and cyclic stability would confine the practical applicability [13]. The aforementioned problems were resolved by integration with some electrically conducting materials like conducting polymers [14, 15], activated carbon [13], and also some metal oxides such as SnO₂ [16], MnO₂ [17], etc. The properties of nanocomposite are different from those of individual metal oxides and could contribute to increase the electrochemical activities. Many α -Fe₂O₃-based nanocomposites have been designed and synthesized for supercapacitor applications. The α -Fe₂O₃ nanomaterials are coupled with some carbon and conducting polymer-based materials α -Fe₂O₃/rGO [18], α -Fe₂O₃/activated carbon [19], α -Fe₂O₃/polyaniline [20] showing enhanced supercapacitance than pristine α -Fe₂O₃. In general, 2D-reduced graphene oxides

have been extensively unutilized as composite materials to improve the electronic conductive, specific capacitance, and rate capability of metal oxide [21]. The enhancement in the specific capacitance of α -Fe₂O₃ is mainly attributed to the higher conductive nature of additive materials [22]. The graphitic structure of graphene was extinguished during the oxidation–reduction process during the chemical oxidation [23]. To resolve prior defects, the ternary composites have been emphasized to improve the specific capacitance and capacitive retention. For instance, Yu et al. fabricated a ternary hierarchical nanosheet of rGO/PANI/Fe₂O₃ with the largest specific capacitance of 605.2 F g⁻¹ at 0.5 A g⁻¹. The improved electrical conductivity with enhanced specific capacitance (37.5 m Fcm⁻² at 20 mAcm⁻²) was achieved compared with pure Fe₂O₃ by Zhao et al. through the formation of Fe₂O₃/RGO/Fe₃O₄ composite [24].

In this paper, we prepared α -Fe₂O₃ nanoparticles, binary α -Fe₂O₃/rGO, and ternary α -Fe₂O₃/SnO₂/rGO nanocomposites by a simple on-spot hydrothermal method. The synthesized materials were used as electrode materials for supercapacitor application in a typical three electrode system. Among the prepared materials, the ternary α -Fe₂O₃/SnO₂/rGO nanocomposites exhibit large specific capacitance with excellent cyclic stability, which can be attributed to improved electrical conductivity and the synergistic effect of α -Fe₂O₃, SnO₂, and rGO. Further, the ACS device was fabricated.

2 Experimental methods

2.1 Materials

Expandable graphite powder, potassium permanganate (KMnO₄), and ammonia solution (NH₃.H₂O, 25–28 wt%) were purchased from Loba Chemie, India. Acetylene black (AR), polyvinylidene fluoride (PVDF, AR), activated carbon, hydrogen peroxide (H₂O₂, 30 wt%), hydrochloric acid (HCl, 36–38 wt%), sulfuric acid (H₂SO₄, 98 wt%), and iron (III) chloride

hexahydrate ($\text{FeCl}_3 \cdot 6\text{H}_2\text{O}$) were purchased from Merck Chemicals, India. Tin (IV) chloride pentahydrate ($> \text{SnCl}_4 \cdot 5\text{H}_2\text{O}$), potassium hydroxide (KOH), poly(vinyl alcohol) (PVA) were purchased from Merck Chemicals, and ethanol (AR) was purchased from HiMedia Laboratories, India. Nickel foam was purchased from Shanghai Zhongwei New Material Co., Ltd, China. All experimental solutions were prepared using DI water. All of the chemicals were analytical grade as used without further purification.

2.2 Synthesis of $\alpha\text{-Fe}_2\text{O}_3$ nanoparticles

In a typical synthesis of $\alpha\text{-Fe}_2\text{O}_3$ nanoparticles, 2.2 g of $\text{FeCl}_3 \cdot 6\text{H}_2\text{O}$ was mixed with 80 mL of DI water under constant magnetic stirring at room temperature. Subsequently, 3 mL of ammonium solution was gently mixed with the above blend and stirred for 1 h to form a homogeneous solution. Next, the resultant solution was transferred into a 50 mL of Teflon-lined stainless steel autoclave and sealed. The autoclave was subjected to hydrothermal treatment at 180 °C for 12 h in a hot-air oven. After the hydrothermal reaction, the autoclave was allowed to cool naturally to room temperature, and the resultant solution was centrifuged with DI water and ethanol to remove the solid product. Finally, the resultant brown product was dried at 80 °C for overnight in a hot-air oven.

2.3 Synthesis of binary $\alpha\text{-Fe}_2\text{O}_3/\text{rGO}$ and $\alpha\text{-Fe}_2\text{O}_3/\text{SnO}_2/\text{rGO}$ nanocomposites

The binary nanocomposites of $\alpha\text{-Fe}_2\text{O}_3/\text{rGO}$ and $\alpha\text{-Fe}_2\text{O}_3/\text{SnO}_2/\text{rGO}$ nanocomposites were prepared by the hydrothermal method. First, the graphene oxide (GO) was prepared by modified Hummer's method as reported in the literature [25, 26]. In a typical synthesis of $\alpha\text{-Fe}_2\text{O}_3/\text{rGO}$ nanocomposite, 0.1 g of as-prepared GO was mixed with 80 mL of DI water under ultrasonic treatment for 2 h to achieve uniform dispersion. Subsequently, 2.2 g of $\text{FeCl}_3 \cdot 6\text{H}_2\text{O}$ was mixed into the GO solution under constant magnetic stirring for 10 min, and then 3 mL of $\text{NH}_3 \cdot \text{H}_2\text{O}$ solution was dropped slowly into the mixture of solution. The resultant solution was allowed to stir for 2 h under magnetic stirring. Next, the resultant solution was transferred into a 50 mL of Teflon-lined stainless steel autoclave, and the sealed autoclave was subjected to the hydrothermal treatment at 180 °C for 12 h in a hot-air oven. After the hydrothermal

reaction, the autoclave was allowed to cool naturally to room temperature and the resultant solution was centrifuged with DI water and ethanol to remove the solid product. Finally, the resultant black product was dried at 80 °C for overnight in a hot-air oven. A similar procedure was followed for the synthesis of ternary $\alpha\text{-Fe}_2\text{O}_3/\text{SnO}_2/\text{rGO}$ nanocomposite with adding of $\text{SnCl}_4 \cdot 5\text{H}_2\text{O}$ precursor into the GO solution [27].

2.4 Material characterization

The crystal structure and phase formation of the prepared samples were studied by powder X-ray diffractometer (XRD) Rigaku Corporation, Japan with $\text{Cu-K}\alpha$ radiation in the 2θ range of 50°–80° at a scanning rate of 2° min^{-1} . The microstructural and morphological characteristics of the prepared materials were revealed using a field emission scanning electron microscope (FESEM, Carl Zeiss, Supra 40) at an accelerating voltage of 15 k and high-resolution transmission electron microscope (HRTEM, JEOL JEM 2100 F microscope) at an accelerating voltage of 200 kV. The elemental compositions of the as-prepared samples were identified by the energy dispersive X-ray analyses (EDS) facility attached with the FESEM instrument. Chemical bonding and functional groups of the prepared materials were analyzed by Fourier transform infrared spectroscopy (FTIR - NEXUS 470 spectrometer) using the KBr pellet method in the range of 4000–450 cm^{-1} . Raman spectra were recorded by LabRAM HR evolution Raman microscopy with UV laser as a light source as an exciting wavelength. X-ray photoelectron spectroscopy (XPS) technique was utilized to characterize the bonding nature and chemical states of materials using ESCA 3400 spectrometer in an ultra-high vacuum with 10 mbar base pressure with monochromatic Al ($\text{K}\alpha$) X-ray source (1486.6 eV).

2.5 Electrochemical measurements

To study the electrochemical performance of the prepared material, the working electrodes were prepared by mixing 80 wt% of active material (As prepared samples), 10 wt% of acetylene black, and 10 wt% of polyvinylidene fluoride (PVDF) as a binder in N-Methyl 1-2-pyrrolidone (NMP) an organic solvent. The obtained homogenous slurry was painted on pre-cleaned nickel foam (1 cm × 1 cm), and

then it was dried at 60 °C for 4 h in a hot-air oven. The acquired electrodes were used for electrochemical studies. The mass loading of active materials on each electrode was measured as 1 mg. The electrochemical studies were performed in a standard three-electrode configuration using Ag/AgCl as a reference electrode, Pt wire as a counter electrode, and as a prepared electrode as a working electrode. All the electrochemical studies were carried out in 6 M KOH electrolyte solution. An ASC device was assembled by sandwiching a Whatman 40 filter paper (soaked in a transparent PVA/KOH gel electrolyte) as a separator in between α -Fe₂O₃/SnO₂/rGO nanocomposite coated nickel foam as the positive electrode (anode) and rGO-coated nickel foam as the negative electrode (cathode) in the Swagelok type cell [28]. The electrochemical techniques such as cyclic voltammetry (CV), galvanostatic charge/discharge (GCD), and electrochemical impedance spectroscopy (EIS) were performed using an electrochemical workstation (Biological SP-150, France). The CV measurement was acquired at various scanning rates (5–100 mVs⁻¹) within the potential window range from 0.05 to 0.5 V. Impedance spectroscopy was measured in the frequency range of 0.01 Hz to 100 kHz with modulating voltage amplitude of ± 10 mV at open circuit potentials (OCP). The specific capacitance of the prepared electrodes was calculated from the following equation using GCD curves [29]:

$$C = \frac{IX\Delta t}{(\Delta mX\Delta V)}, \quad (1)$$

where I is applied current (A), Δt represents discharge time (s), ΔV (V) is the sweep potential window following time intervals, and m (g) is the mass of the active materials for a three-electrode system.

For a two-electrode system, the specific capacitance was calculated using the following equations [30]:

$$C_s = \frac{2}{mv^2} \int iV(t)dt. \quad (2)$$

The energy density (E) and power density (P) derived from galvanostatic tests can be calculated from the following equation:

$$E = \frac{C(\Delta V)^2}{2}, \quad (3)$$

$$P = \frac{E}{\Delta t}, \quad (4)$$

where C_s (F/g) is the specific capacitance of the supercapacitor, I (A) corresponds to the discharge current, ΔV (V) is the potential window, Δt (s) is the discharge time, and m (g) refers to the total active mass of ASC(Positive and negative) materials [31].

3 Results and discussion

The synthesis of binary α -Fe₂O₃/rGO and ternary α -Fe₂O₃/SnO₂/rGO nanocomposites by the hydrothermal process is typically illustrated in Fig. 1. In general, GO has more negatively charged ions such as hydroxyl and epoxy groups in planes and carboxyl groups on their edges, and so it is uniformly dispersed into water. The positively charged metal ions (Fe³⁺ and Sn⁴⁺) in the GO solution can selectively be attached to a negatively charged surface functional group of GO sheets [26, 27]. In the present case surface, the functional group of GO sheets acted as nucleation sites in the alkaline solution (NH₃-H₂O) to form Fe(OH)₃ and Sn(OH)₄ and subsequent hydrothermal treatment metal hydroxides were transformed as α -Fe₂O₃ and SnO₂ nanoparticles.

The powder X-ray diffraction (XRD) measurement was carried out to investigate the phase purities and crystal structure of the as-prepared samples. The average crystallite size of the α -Fe₂O₃ was determined by the full width at half maximum (FWHM) of the X-ray diffraction peak using Scherer's Eq. (5) as follows:

$$D = \frac{k\lambda}{\beta \cos\theta}, \quad (5)$$

where D —crystallite size, λ —X-ray wavelength, β —FWHM of the diffraction peak, θ —diffraction angle, and k —Scherer's constant of the order of unity. Figure 2 shows the XRD patterns of α -Fe₂O₃ nanoparticles, binary α -Fe₂O₃/rGO, and ternary α -Fe₂O₃/SnO₂/rGO nanocomposites. The diffraction peaks at 24.13°, 33.15°, 35.61°, 40.85°, 49.48°, 54.09°, 57.79°, 62.45°, 63.99°, 69.60°, and 71.93° correspond to the (012), (104), (110), (113), (024), (116), (018), (214), (300), (208), and (1010) plane of rhombohedral α -Fe₂O₃ (JCPDS card No. 33-0664, respectively). In the ternary composition, the peaks at 26.61°, 33.89°, 38.96°, 42.63°, and 57.82° correspond to the (110), (101), (111), (210), and (002) plane of tetragonal SnO₂ (JCPDS card No. 41-1445) along with characteristic peaks of α -Fe₂O₃ which confirms the formation of the ternary

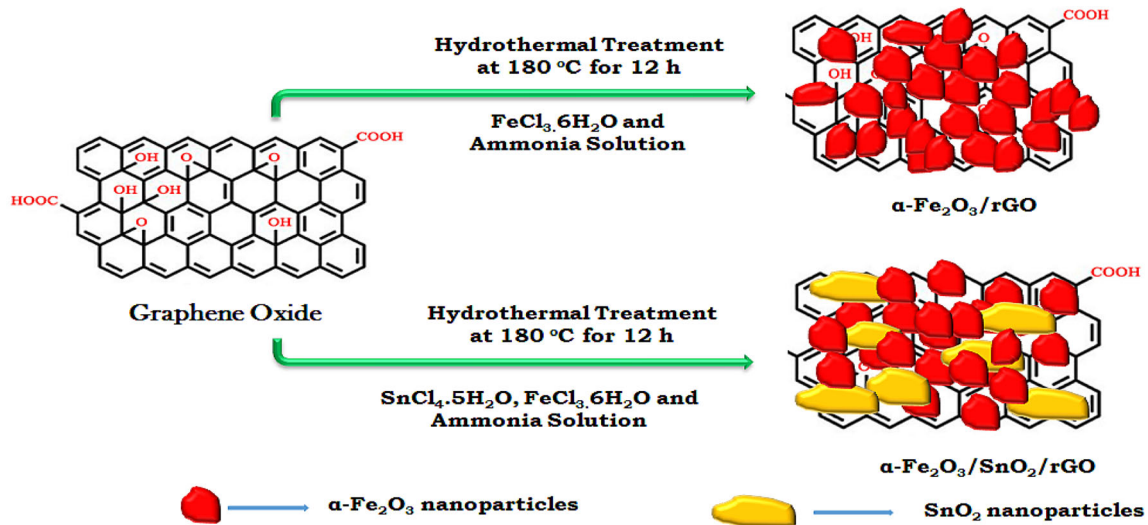


Fig. 1 Schematic illustration for preparation of binary $\alpha\text{-Fe}_2\text{O}_3/\text{rGO}$ and ternary $\alpha\text{-Fe}_2\text{O}_3/\text{SnO}_2/\text{rGO}$ nanocomposites by hydrothermal method

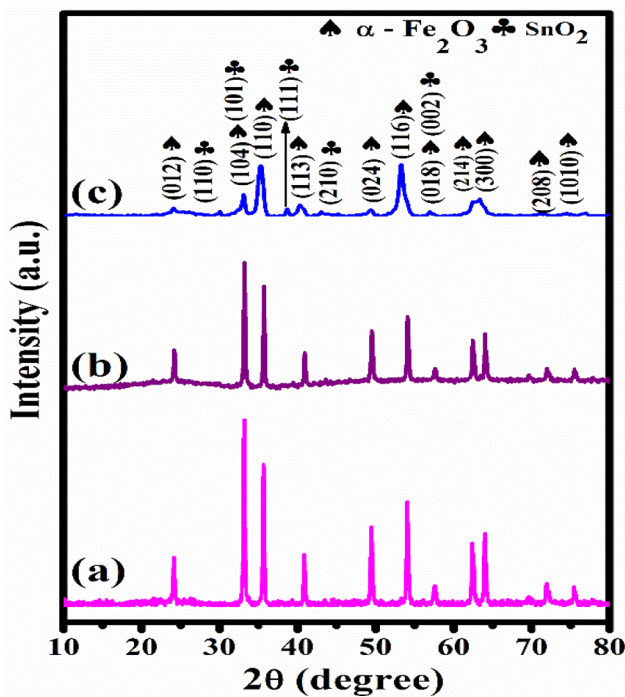


Fig. 2 Powder XRD patterns of **a** $\alpha\text{-Fe}_2\text{O}_3$ nanoparticles, **b** binary $\alpha\text{-Fe}_2\text{O}_3/\text{rGO}$, and **c** ternary $\alpha\text{-Fe}_2\text{O}_3/\text{SnO}_2/\text{rGO}$ nanocomposite

nanocomposite. The crystallite size was estimated by using the reflections of characteristic planes such as to (110), and the crystallite size is calculated as 12.7 nm for the prepared samples of $\alpha\text{-Fe}_2\text{O}_3$. The characteristic peak of GO at $2\theta = 11.6^\circ$ is diapered in both binary $\alpha\text{-Fe}_2\text{O}_3/\text{rGO}$, and ternary $\alpha\text{-Fe}_2\text{O}_3/\text{SnO}_2/\text{rGO}$ nanocomposites inferred that the

successful reduction of GO during the hydrothermal synthesis of nanocomposites. Meanwhile, the characteristic peak for rGO was not detected in the composite materials due to the presence of a low quantity of rGO [32].

The optical properties of the nanocomposite were studied by UV–Vis. measurements. The UV–Vis. absorbance spectra of $\alpha\text{-Fe}_2\text{O}_3$ nanoparticles, binary $\alpha\text{-Fe}_2\text{O}_3/\text{rGO}$, and $\alpha\text{-Fe}_2\text{O}_3/\text{SnO}_2/\text{rGO}$ ternary nanocomposites are displayed in Fig. 3a. The band gap of the samples was estimated by the following equation:

$$\alpha = \frac{A(E_g - h\nu)^n}{h\nu}, \tag{6}$$

where absorption coefficient (α), Planck’s constant (h), frequency of vibration (ν), $n = 1/2$ for indirect transition, band gap (E_g), and proportional constant (A). The calculated band gaps of $\alpha\text{-Fe}_2\text{O}_3$ nanoparticles, binary $\alpha\text{-Fe}_2\text{O}_3/\text{rGO}$, and $\alpha\text{-Fe}_2\text{O}_3/\text{SnO}_2/\text{rGO}$ ternary nanocomposites are shown Fig. 3b [33]. The calculated band gaps of $\alpha\text{-Fe}_2\text{O}_3$ nanoparticles, binary $\alpha\text{-Fe}_2\text{O}_3/\text{rGO}$, and $\alpha\text{-Fe}_2\text{O}_3/\text{SnO}_2/\text{rGO}$ ternary nanocomposites were 1.9 eV, 1.86 eV, and 1.8 eV, respectively. It is expected that the reduction in the band-gap energy increases the electrical conductivity of the materials [34, 35]. Therefore, the electrical conductivity of the $\alpha\text{-Fe}_2\text{O}_3/\text{SnO}_2/\text{rGO}$ ternary nanocomposite was higher than that of pure $\alpha\text{-Fe}_2\text{O}_3$ nanoparticles and binary $\alpha\text{-Fe}_2\text{O}_3/\text{rGO}$

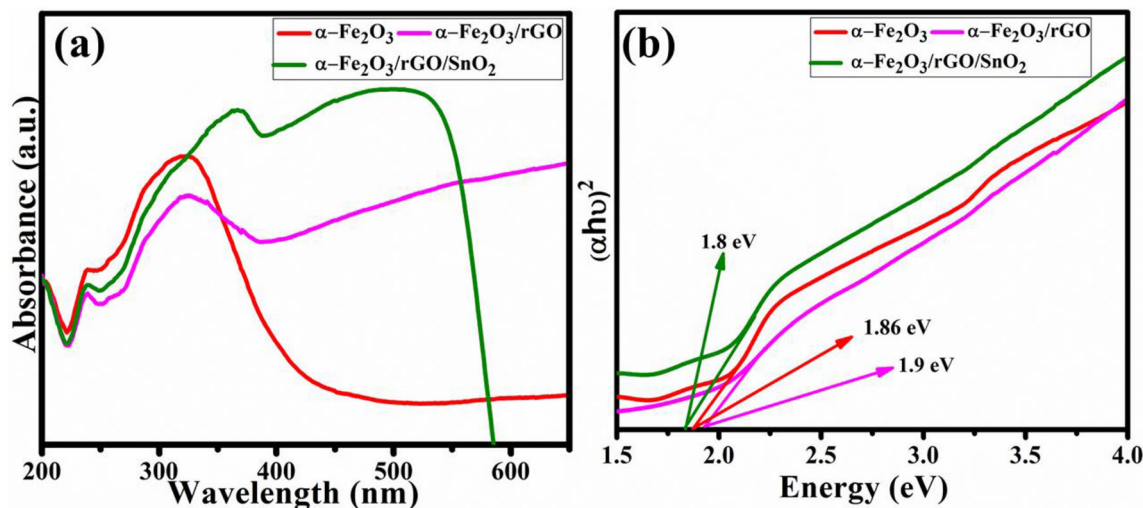


Fig. 3 **a** UV–vis absorption spectra, **b** tauc plot for α -Fe₂O₃ nanoparticles, binary α -Fe₂O₃/rGO, and ternary α -Fe₂O₃/SnO₂/rGO nanocomposite

nanocomposite. Thus, the specific capacitance of the materials is increased [36].

The surface morphology of the synthesized samples was characterized by the field emission scanning electron microscope (FESEM). Figure 4 represents the FESEM image of α -Fe₂O₃ nanoparticles, binary α -Fe₂O₃/rGO, and α -Fe₂O₃/SnO₂/rGO ternary nanocomposites. The α -Fe₂O₃ nanoparticles with a size of \sim 12 nm were agglomerated to form the spherical shape (Fig. 4a). The agglomeration of the nanoparticles is mainly attributed to an association of high surface energy with smaller particles [37]. The measured particle of α -Fe₂O₃ material was well consistent with the XRD result. Figure 4b displays the morphology of binary α -Fe₂O₃/rGO, which suggests that the uniform size α -Fe₂O₃ nanoparticles were embedded on 2D rGO sheets. As shown in Fig. 4c, both α -Fe₂O₃ and SnO₂ nanoparticles were strongly

embedded on rGO sheets which were distinguished by their particle size and [27].

The internal structure and morphology of the ternary α -Fe₂O₃/SnO₂/rGO nanocomposite were further characterized by TEM and HRTEM imaging techniques. Figure 5a and b displays the distinguished morphology of rod and spherical shapes which are in the agglomerated form. The length and diameter of the rod shape particles were measured as \sim 60–70 nm and \sim 10–15 nm, respectively. The HRTEM image was exploited to distinguish the two different crystal phases in a single system of the composite. HRTEM image of ternary α -Fe₂O₃/SnO₂/rGO nanocomposite depicted in Fig. 4b demonstrates that the presence of two distinguished crystals with well-ordered crystal planes and lattice spacing was measured as 0.36 nm and 0.32 nm, which are ascribed to (012) and (111) planes of α -Fe₂O₃ and SnO₂

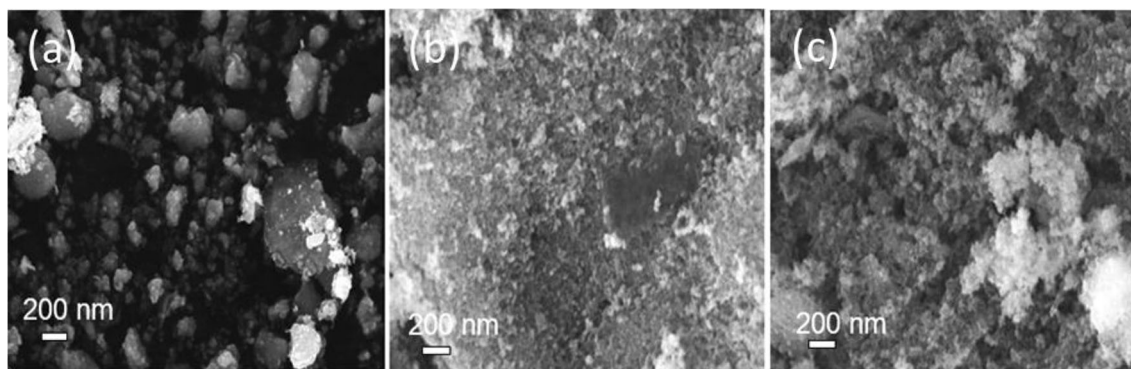


Fig. 4 FESEM images **a** α -Fe₂O₃ nanoparticles, **b** binary α -Fe₂O₃/rGO, and **c** ternary α -Fe₂O₃/SnO₂/rGO nanocomposites

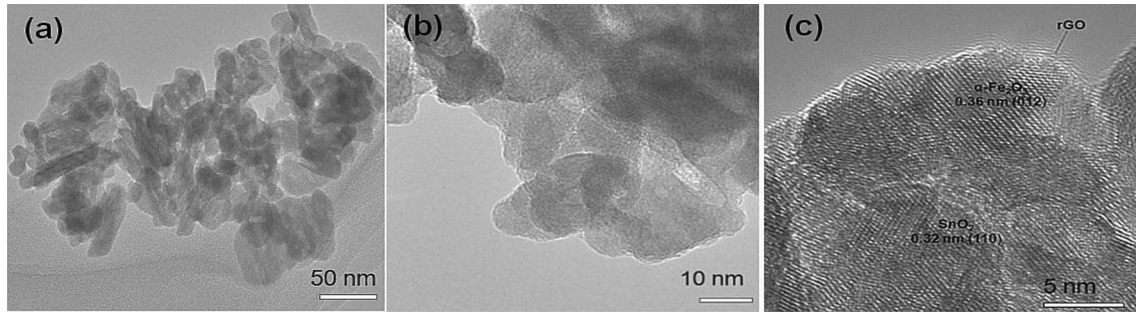


Fig. 5 a, b TEM and c HRTEM images ternary $\alpha\text{-Fe}_2\text{O}_3/\text{SnO}_2/\text{rGO}$ nanocomposite

crystal planes, respectively [38, 39]. Moreover, the rGO sheet was attached at the edge of the nanoparticles which is indicated by a red arrow mark in the HRTEM image. Therefore, the formation of the ternary $\alpha\text{-Fe}_2\text{O}_3/\text{SnO}_2/\text{rGO}$ nanocomposite was confirmed by FESEM and HRTEM characterizations.

As shown in Fig. 6, the chemical composition of the prepared material was identified by EDS techniques. Figure 6a& b reveals that the presence of a stoichiometric quantity of Fe and O in $\alpha\text{-Fe}_2\text{O}_3$ and C, Fe, and O in $\alpha\text{-Fe}_2\text{O}_3/\text{rGO}$. Further, Fig. 6c evidences that the presence of Fe, Sn, O, and C in the ternary $\alpha\text{-Fe}_2\text{O}_3/\text{SnO}_2/\text{rGO}$ nanocomposite. The functional groups of the prepared material were studied by FTIR spectroscopy. Figure 7 shows the FTIR spectra of $\alpha\text{-Fe}_2\text{O}_3$ nanoparticles binary $\alpha\text{-Fe}_2\text{O}_3/\text{rGO}$ and ternary $\alpha\text{-Fe}_2\text{O}_3/\text{SnO}_2/\text{rGO}$ nanocomposites. The strong bands

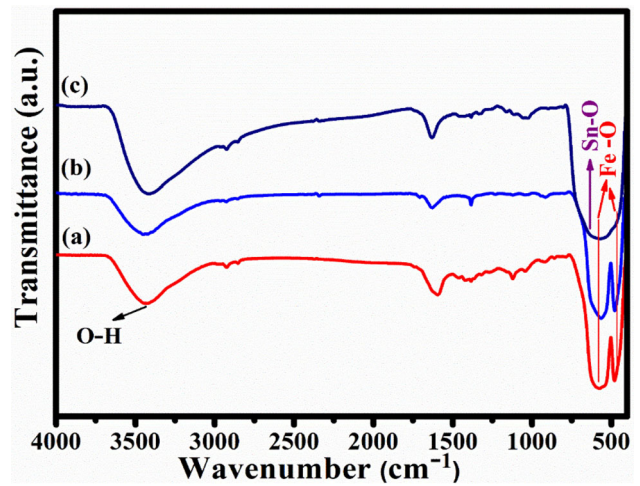


Fig. 7 FTIR spectra of a $\alpha\text{-Fe}_2\text{O}_3$ nanoparticles, b binary $\alpha\text{-Fe}_2\text{O}_3/\text{rGO}$, and c ternary $\alpha\text{-Fe}_2\text{O}_3/\text{SnO}_2/\text{rGO}$ nanocomposites

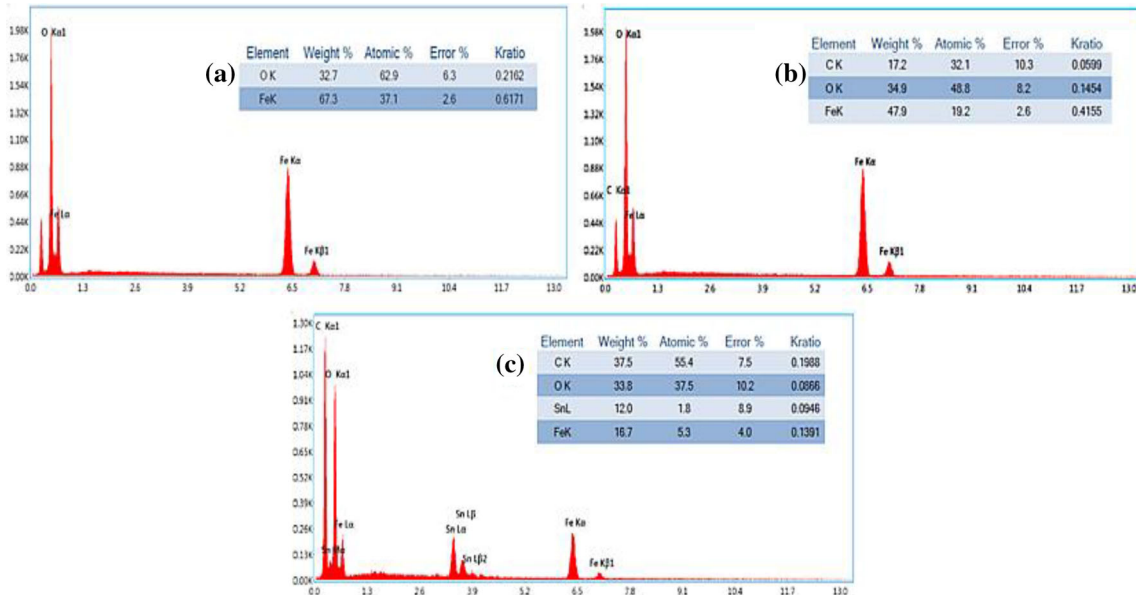


Fig. 6 EDS spectra of a $\alpha\text{-Fe}_2\text{O}_3$ nanoparticles, b binary $\alpha\text{-Fe}_2\text{O}_3/\text{rGO}$, and c ternary $\alpha\text{-Fe}_2\text{O}_3/\text{SnO}_2/\text{rGO}$ nanocomposites. The inset table shows the stoichiometric quantity of elements in the respective material

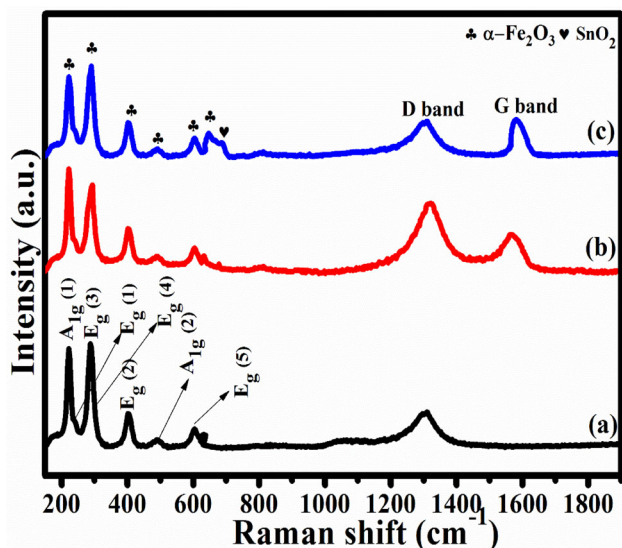


Fig. 8 Raman spectra of **a** α -Fe₂O₃ nanoparticles, **b** binary α -Fe₂O₃/rGO, and **c** ternary α -Fe₂O₃/SnO₂/rGO nanocomposite

at 575 cm⁻¹ and 477 cm⁻¹ could be attributed to stretching vibrations of Fe-O in FeO₆ octahedron and FeO₄ tetrahedron structures of α -Fe₂O₃ [40]. Along with the Fe-O vibration, the strongest peak at 627 cm⁻¹ was assigned to the Sn-O bond of SnO₂ in the ternary α -Fe₂O₃/SnO₂/rGO nanocomposites [41]. The peak related to the GO cannot be detected in the

FTIR spectra of binary α -Fe₂O₃/rGO, and ternary α -Fe₂O₃/SnO₂/rGO nanocomposites confirm the successful reduction of GO into rGO. Further, the new peak was found at 1570 cm⁻¹ in the binary α -Fe₂O₃/rGO, and ternary α -Fe₂O₃/SnO₂/rGO nanocomposites could be assigned to the C=C vibration of rGO [42]. Moreover, the broadband at 3420 cm⁻¹ was assigned to the O-H vibration of surface absorbed water molecules. The formation of nanocomposite was further confirmed by the Raman spectroscopy technique. The Raman spectra of α -Fe₂O₃ nanoparticles, binary α -Fe₂O₃/rGO, and ternary α -Fe₂O₃/SnO₂/rGO nanocomposite are shown in Fig. 8. The fundamental vibration of α -Fe₂O₃ assigned at 224, 287, 403, 494, 606, 653, and 1320 cm⁻¹ in Raman spectra of α -Fe₂O₃ nanoparticles (Fig. 8a). The peaks at 224 and 494 cm⁻¹ were attributed to A_{1g} symmetry modes α -Fe₂O₃ and the vibration bands at 287, 403, and 606, 653, and 1320 cm⁻¹ were ascribed for E_g symmetry [43]. As shown in Fig. 8b and c, two strong peaks at 1582 and 1319 cm⁻¹ correspond to the 'D' and 'G' band of GO were stretched with the fundamental vibration modes of α -Fe₂O₃ [44, 45]. Here, the D band is related to the disordered atomic arrangement due to sp³ hybridization. Meanwhile, the G band can be attributed to the plane vibration of the sp²-carbon atom [46]. Moreover, the peak at 697 cm⁻¹

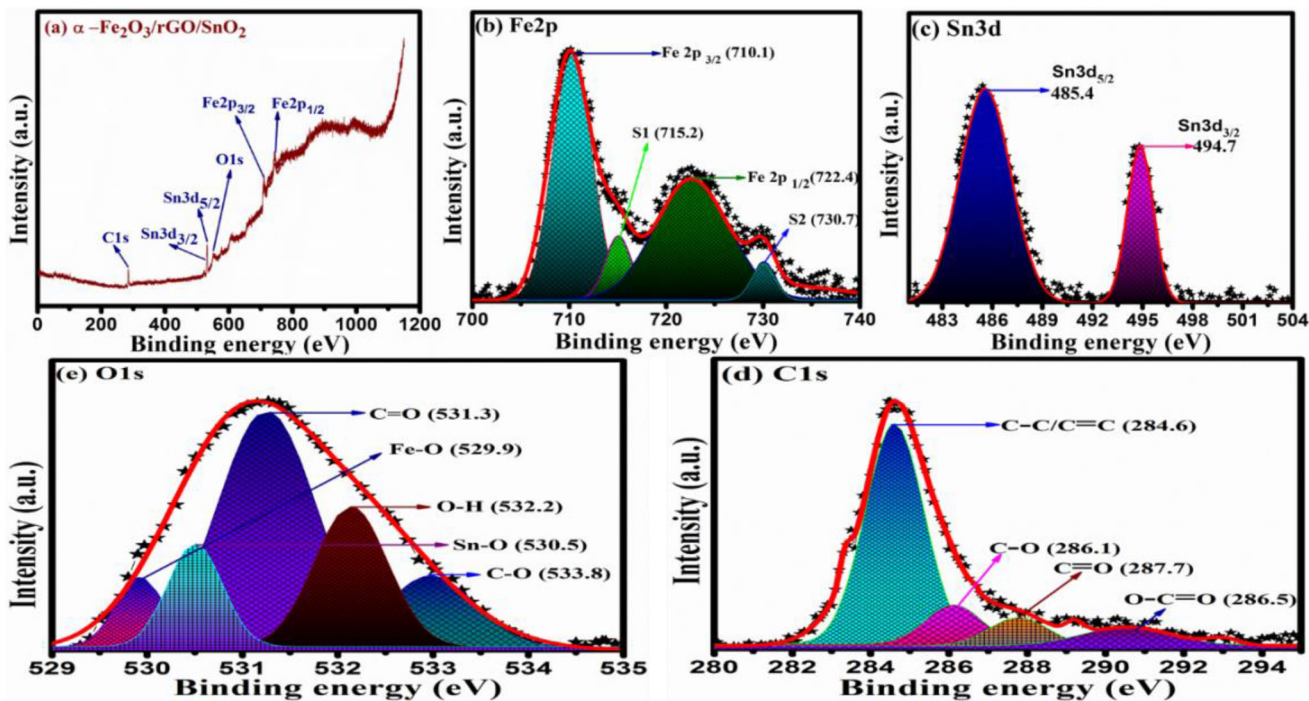


Fig. 9 XPS spectra of **a** survey spectra, **b** Fe 2p, **c** Sn 3d, **d** C 1s, and **e** O 1s for ternary α -Fe₂O₃/SnO₂/rGO nanocomposites

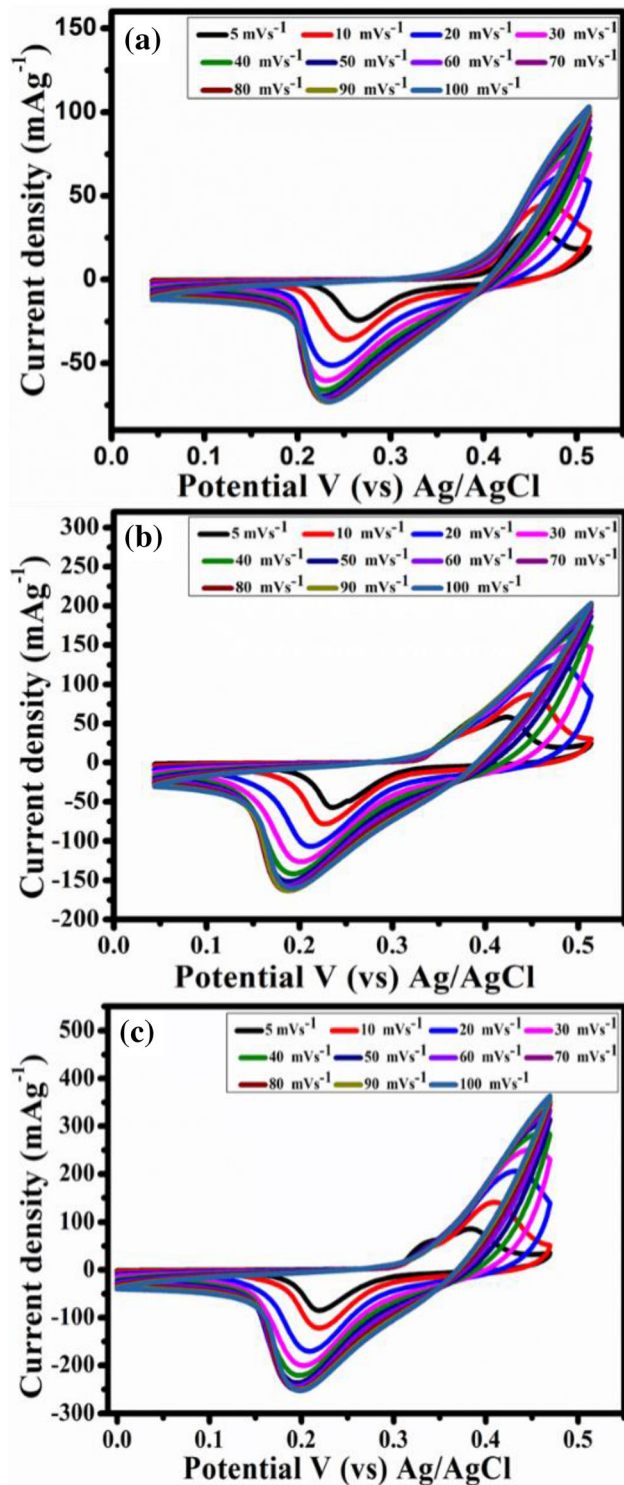


Fig. 10 CV curves of **a** α -Fe₂O₃ nanoparticles, **b** binary α -Fe₂O₃/rGO, and **c** ternary α -Fe₂O₃/rGO/SnO₂ nanocomposite for different scanning rates between 5 and 100 mV s⁻¹

in the Raman spectra of ternary α -Fe₂O₃/SnO₂/rGO nanocomposite was assigned to the SnO₂ [47]. The co-

existence of vibration modes of α -Fe₂O₃, SnO₂, and rGO in the Raman spectrum of ternary α -Fe₂O₃/SnO₂/rGO nanocomposite confirms the formation of the ternary nanocomposite.

The chemical and oxidation states of the ternary α -Fe₂O₃/SnO₂/rGO nanocomposite were further examined by XPS measurement. The full survey spectrum of ternary α -Fe₂O₃/SnO₂/rGO nanocomposite shown in Fig. 9a reveals the co-existence of Fe, Sn, C, and O elements. Figure 9b displays core-level spectra of Fe2p, consists of two peaks at 710.1 eV and 722.4 eV for Fe 2p_{3/2} and to Fe 2p_{1/2}, respectively, and correspond to the trivalent Fe³⁺ oxidation state of α -Fe₂O₃ [48]. Meanwhile, the two peaks at 485.4 and 494.7 eV were assigned to Sn 3d_{5/2} and Sn 3d_{3/2}, respectively, which confirm the Sn⁴⁺ oxidation state of SnO₂ (Fig. 9c) [49]. The core-level spectra of C 1s (Fig. 9d) were further deconvoluted into four peaks, centered at 284.6, 286.1, 286.7, and 286.5 eV from the chemical bond of C–C, C–O, C=O, and O–C=O, respectively [50]. Further, the core-level spectrum of O 1s in Fig. 9e is divided into five peaks at 529.9, 530.5, 531.3, 532.2, and 533.8 eV, corresponding to the surface oxygen-containing group for Fe–O, Sn–O, C=O, O–H, and C–O, respectively [51]. The shifting in the peak position of Fe, Sn, O, and C from its original values may be due to the strong interaction between rGO, α -Fe₂O₃, and SnO₂ [52]. The result inferred that the electrostatic interactions were developed between oxygen atoms in metal oxide surfaces with rGO [53, 54].

To evaluate the electrochemical performance of the prepared samples, CV and GCD measurements were carried out in typical three electrodes in 6 M KOH solution. Figure 10 shows the CV curves of α -Fe₂O₃ nanoparticles, binary α -Fe₂O₃/rGO, and ternary α -Fe₂O₃/SnO₂/rGO nanocomposites for different scanning rates between 5 and 100 mV s⁻¹ within the potential window of 0.05 to 0.5 V. All CV curves show a two pairs Faradaic redox reaction peak in the cathodic and anodic regions which revealed a pseudo-capacitance behavior of prepared electrode materials [44, 47].

The current density in CV curves of all prepared materials linearly depends on scanning rates in both anodic and cathodic sides, which implies the ideal capacitive behavior of electrodes. It is obvious that the anodic peaks shift towards the positive potential direction and the cathodic peaks shift towards the negative potential direction upon increasing the

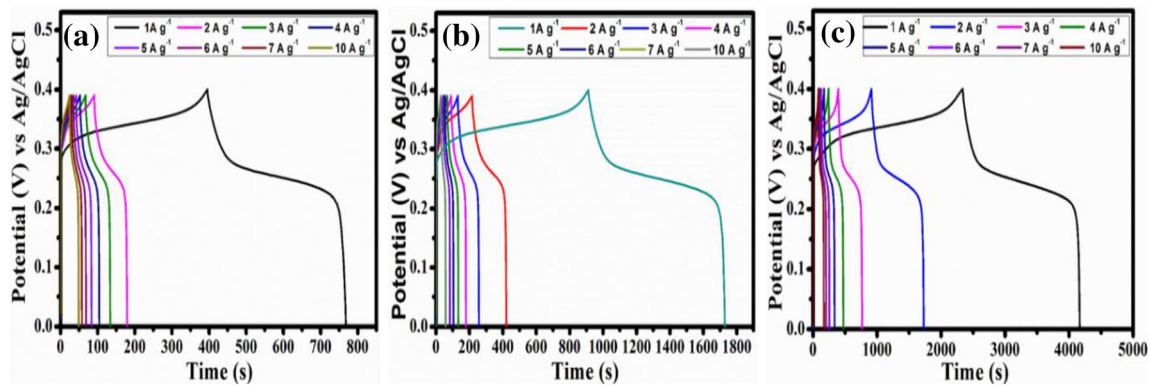


Fig. 11 GCD curves **a** α -Fe₂O₃ nanoparticles, **b** binary α -Fe₂O₃/rGO, and **c** ternary α -Fe₂O₃/rGO/SnO₂ nanocomposites at different current densities

scanning rate. Although the redox peaks position was conserved at high scanning rates due to the fast electronic and ionic movements at the surface of the electrode [3]. The GCD curves for α -Fe₂O₃ nanoparticles, binary α -Fe₂O₃/rGO, and ternary α -Fe₂O₃/SnO₂/rGO nanocomposites in the voltage range of 0–0.4 V at different current densities are shown in Fig. 11. The pseudocapacitive behavior of all prepared materials was confirmed from voltage plateaus, which is in good agreement with CV measurement.

Figure 12a displays comparative CV curves of α -Fe₂O₃ nanoparticles, binary α -Fe₂O₃/rGO, and ternary α -Fe₂O₃/rGO/SnO₂ nanocomposites at a scanning rate of 5 mV/s in the potential range between 0.05 and 0.5 V. The ternary α -Fe₂O₃/rGO/SnO₂ nanocomposites exhibit a larger area under CV curve than α -Fe₂O₃ nanoparticles and binary α -Fe₂O₃/rGO, demonstrating a notable enhancement in specific capacitance of ternary α -Fe₂O₃/rGO/SnO₂ nanocomposites. As shown in Fig. 12b, the GCD curves of the α -Fe₂O₃ nanoparticles, binary α -Fe₂O₃/rGO, and ternary α -Fe₂O₃/rGO/SnO₂ nanocomposites at a constant current density of 1 A g⁻¹ were compared. As expected that α -Fe₂O₃/rGO/SnO₂ nanocomposites exhibit the longest discharge time than that of other prepared materials due to their enhanced electrochemical property [55]. The specific capacitance of the prepared materials was calculated from respective GCD curves at different current densities as illustrated in Fig. 12c. The volumetric specific capacitance of ternary α -Fe₂O₃/rGO/SnO₂ nanocomposites was calculated as 821 Fg⁻¹ for current densities of 1 A g⁻¹, 793 Fg⁻¹ (2 A g⁻¹), 765 Fg⁻¹ (3 A g⁻¹), 731 Fg⁻¹ (4 A g⁻¹), 696 Fg⁻¹ (5 A g⁻¹), 651

Fg⁻¹ (6 A g⁻¹), 609 Fg⁻¹ (7 A g⁻¹), and 501 Fg⁻¹ (10 A g⁻¹), respectively. As expected, the ternary α -Fe₂O₃/rGO/SnO₂ nanocomposites provide higher specific capacitance than that of α -Fe₂O₃ nanoparticles and binary α -Fe₂O₃/rGO nanocomposite. The specific capacitance of the ternary composite at a constant current density of 1 A g⁻¹ is comparatively higher than that of other materials (Fig. 12d).

Further, the electrochemical impedance spectroscopy (EIS) measurement was conducted to study the ionic diffusion and electronic conductivity of all prepared electrodes. The Nyquist plots (Fig. 12e) for prepared electrodes were composed of the semicircle at the high-frequency region and a straight line at the low-frequency region [56]. The Nyquist curves were fitted based on the equivalent circuit model, and the fitted circuit was displayed in the inset of Fig. 12e. In general, the intercept of Nyquist plots on the real axis at the high-frequency region provides internal resistance (R_s) occurring from intrinsic resistance of current collector and electrode materials, ionic resistance of the electrolyte, and contact resistance between the electrode material and current collector [57]. Meanwhile, the charge transfer resistance (R_{ct}) arises from the conductivity difference between the solid electrode and liquid electrolyte and the slope of the straight in the low-frequency region related to the diffusion resistance (W) [58]. The values of R_{ct} for prepared electrodes were obtained by fitting the Nyquist plots data by Zview. The calculated R_{ct} values are 35.84, 24.73, and 18.66 Ω for α -Fe₂O₃ nanoparticles, binary α -Fe₂O₃/rGO, and α -Fe₂O₃/rGO/SnO₂ nanocomposites, respectively. The ternary α -Fe₂O₃/rGO/SnO₂ nanocomposites show a lower charge transfer resistance (R_{ct}) than other materials

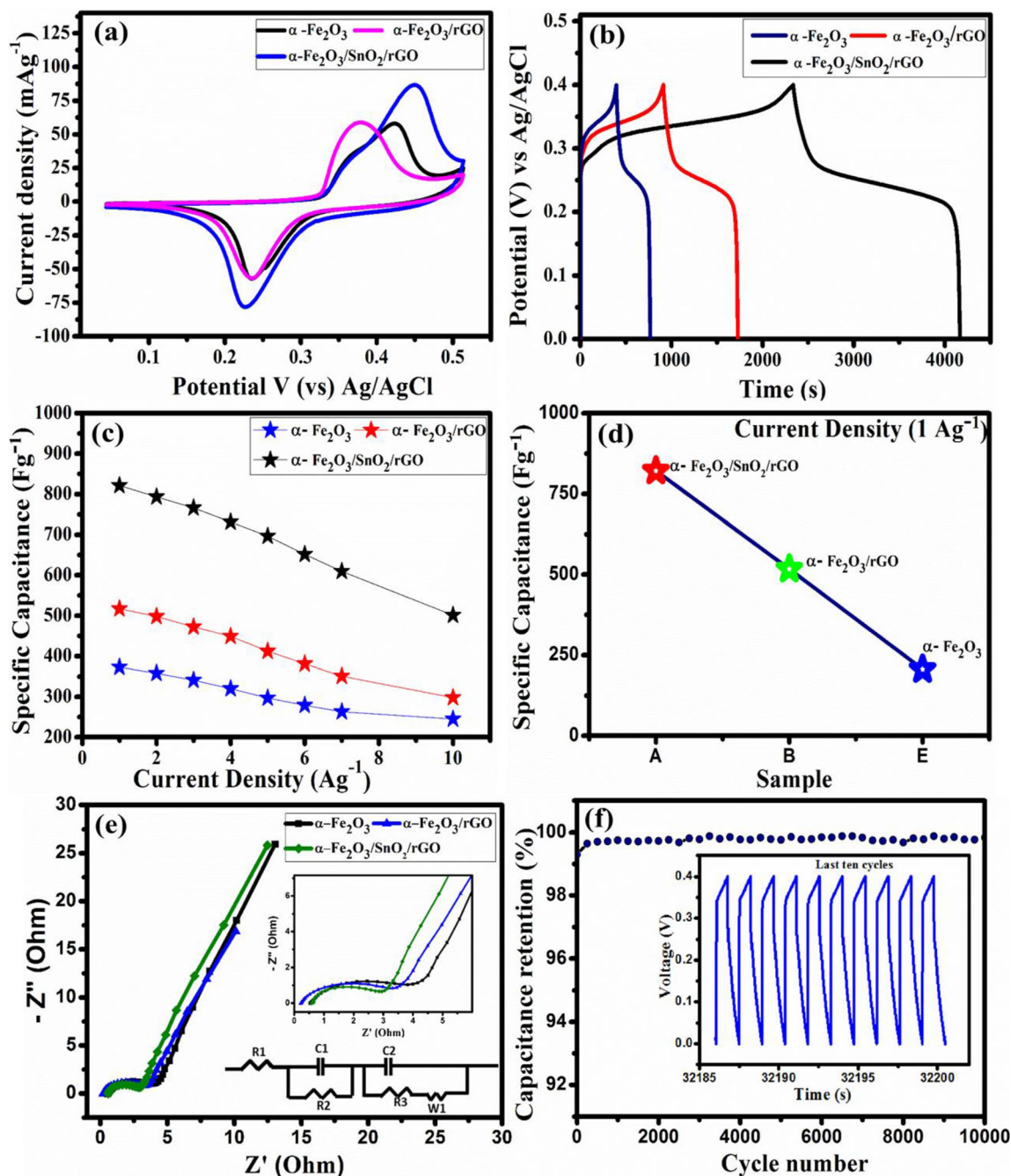
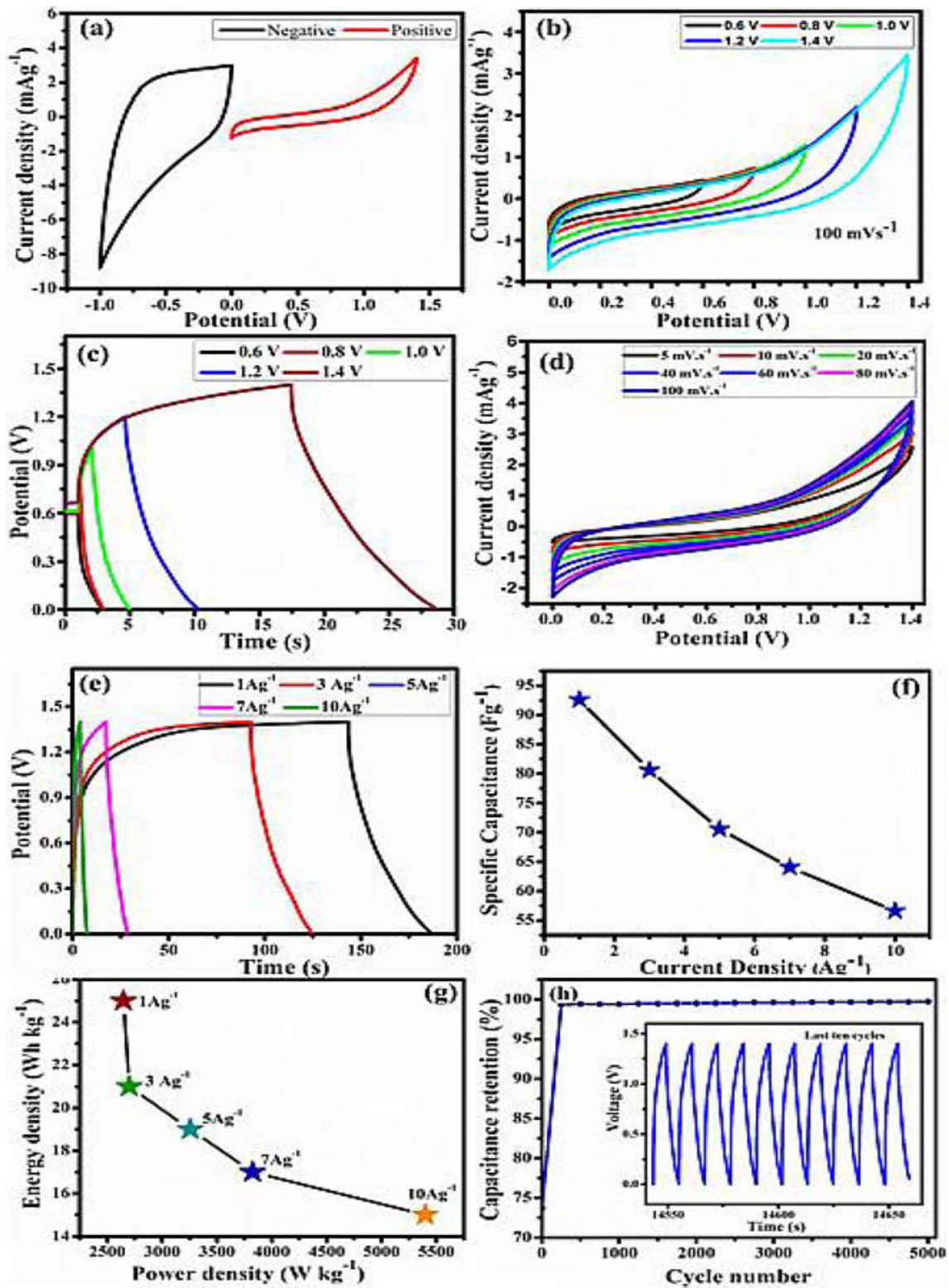


Fig. 12 a Comparison of CV curves of α -Fe₂O₃ nanoparticles, binary α -Fe₂O₃/rGO, and ternary α -Fe₂O₃/rGO/SnO₂ nanocomposites at a scan rate of 5 mV/s. b Comparison of GCD curves of α -Fe₂O₃ nanoparticles, binary α -Fe₂O₃/rGO, and ternary α -Fe₂O₃/rGO/SnO₂ nanocomposites at current densities 1 A g⁻¹. c The gravimetric specific capacitance of α -Fe₂O₃ nanoparticles, binary α -Fe₂O₃/rGO, and ternary α -Fe₂O₃/rGO/SnO₂ nanocomposites at different current densities. d Comparison of

specific capacitance of α -Fe₂O₃ nanoparticles, binary α -Fe₂O₃/rGO, and ternary α -Fe₂O₃/rGO/SnO₂ nanocomposites at a constant current density of 1 A g⁻¹. e Nyquist plots of α -Fe₂O₃ nanoparticles, binary α -Fe₂O₃/rGO, and ternary α -Fe₂O₃/rGO/SnO₂ nanocomposites. Inset shows the equivalent circuit model and a magnified view of Nyquist plots in the high-frequency region. f Cycle performance of ternary α -Fe₂O₃/rGO/SnO₂ nanocomposites at a current density of 10 A g⁻¹



◀ **Fig. 13** Electrochemical performance of α -Fe₂O₃/rGO/SnO₂ nanocomposites-based asymmetric supercapacitor (a). CV curves for different scanning rates between 5 and 100 mV s⁻¹, b Comparison of GCD curves at different current densities, c CV curves at different potential windows at 100 mVs⁻¹, d GCD curves at different potential windows at a fixed current density of 7 Ag⁻¹. e Specific capacitance at different current densities. f Ragone plots at a current density of 1 A g⁻¹. g Cycle performance at a current density of 10 A g⁻¹ i Cycle performance at a current density of 10 A g⁻¹ of ASC device

due to their higher electrical conductivity [59]. Furthermore, a more vertical line in the low-frequency region with a higher slope for the α -Fe₂O₃/rGO/SnO₂ nanocomposites indicates the faster ion diffusion rate [27]. The cyclic stability test was performed to study the practical feasibility of the electrode material. Figure 12f depicts the electrochemical cyclic stability of the α -Fe₂O₃/rGO/SnO₂ nanocomposites for 10,000 GCD cycles at the current density of 10 A g⁻¹. The specific capacitance retention of the α -Fe₂O₃/rGO/SnO₂ nanocomposites is 98.7% after 10,000 GCD cycles. The higher capacitance retention is mainly due to the lower charge transfer resistance of ternary nanocomposite [60]. The outstanding electrochemical performances of the α -Fe₂O₃/rGO/SnO₂ nanocomposites are mainly attributed by the following virtues:

- (1) The α -Fe₂O₃ nanoparticles are embedded on high surface area nanosheets provide abundant electrochemical active sites, increases the accessible surface area, and lead to enhancement in the electrochemical reaction kinetics.
- (2) The conductive rGO backbone in the nanocomposite extremely improved the electrical conductivity which hinders the charge transfer resistance and promoted the rapid electron transfer process.
- (3) The SnO₂ nanoparticles in the composite matrix further increased the electrical conductivity and mechanical strength of the whole system, thus, enhancing the electrochemical performances and cyclic stability.

Further, the practical usage of α -Fe₂O₃/rGO/SnO₂ electrode material was verified by assembling of ASC device using the as-prepared material on NF as a positive electrode and rGO on NF as a negative electrode with Whatman 40 filter as a separator and PVA/6 M KOH as a gel electrolyte. First, the

potential windows of both positive (α -Fe₂O₃/rGO/SnO₂) and negative (activated carbon) electrodes were separately identified by CV measurement, as shown in Fig. 13a. To establish the stable operating potential window of the ASC device, the CV curves were recorded within the different potential windows from 0 to 0.6 V, 0 to 0.8 V, 0 to 1.0 V, 0 to 1.2 V, and 0 to 1.4 V) at 100 m Vs⁻¹ and similarly, GCD curves were recorded at 1 Ag⁻¹ (Fig. 13b and c). Figure 13d depicts the CV curves of ASC at different potential scan rates (0.6 V, 0.8 V, 1.0 V, 1.2 V, and 1.4 V) within the potential window of 0.0–1.4 V. The shape of the curves does not change much with increasing scan rate, suggesting good reversibility for the electrode materials. Moreover, the CGD curves were obtained within the different potential windows like CV measurement at different scanning rates (1, 3, 5, 7, and 10 A g⁻¹), shown in Fig. 13e. It can be observed that the ASC demonstrates stable electrochemical behavior with excellent reversibility within the potential window of 0 to 1.4 V. The specific capacitances of the ASC were calculated for different current densities using Eq. 2, shown in Fig. 13f. ASC has exhibited the highest specific capacitance of 92.6 Fg⁻¹ at a current density of 1 Ag⁻¹. Further, the energy and power densities of assembled ASC are calculated using Eq. 3 and Eq. 4, respectively. Figure 13 g shows the plot between calculated power and energy densities for different applied current densities. ASC can deliver the highest energy density of 25 Wh kg⁻¹ at a power density of 2647 Wkg⁻¹ for an applied current density of 1 A g⁻¹. The cycle life of the ASC has investigated up to 5000 GCD cycles at a current density of 10 A g⁻¹, and corresponding capacitance retention data are plotted in Fig. 13h.

4 Conclusions

In summary, we reported a synthesis of α -Fe₂O₃ nanoparticles, binary α -Fe₂O₃/rGO, and ternary α -Fe₂O₃/SnO₂/rGO nanocomposites by a one-step hydrothermal method for supercapacitor applications. The ternary α -Fe₂O₃/SnO₂/rGOnanocomposite provided a higher specific capacitance 821 Fg⁻¹ at a current density of 1Ag⁻¹ than α -Fe₂O₃ nanoparticles and binary α -Fe₂O₃/rGO nanocomposite. Each component in the ternary α -Fe₂O₃/SnO₂/rGO nanocomposite played an important role to improve the specific capacitance. Reduced graphene oxide has

been contributed to improving the electrical conductivity and surface of the nanocomposite, and SnO₂ nanoparticles in the composite also improved the electrical conductivity and specific capacitance. Moreover, the ternary nanocomposite maintains 98.7% retention of the first cycle capacity after 10,000 cycles at 10 A g⁻¹. The assembled ASC has an attractive specific capacitance, energy densities, and power densities within a potential window of 0.0–1.4 V in the alkaline polymer electrolyte and exhibits almost 92.59% capacitance retention during 5000 cycles. These results demonstrated that the ternary α -Fe₂O₃/SnO₂/rGO nanocomposite would be the potential and promising supercapacitor electrode materials.

Acknowledgements

The authors would like to acknowledge the Ministry of Science and Technology, Department of Science and Technology (WOS-A) (File No. SR-WOS-A/PM-71/2017), and DST-SERB, India (File No. EMR/2017/001238), for financial support and the authors extend their appreciation to the Deanship of Scientific Research at King Khalid University for funding this study through the Large Research Group Project under grant number R.G.P. 2/139/1442.

References

- J. Libich, J. Máca, J. Vondrák, O. Čech, M. Sedlářková, Supercapacitors: properties and applications. *J. Energy Storage*. **17**, 224–227 (2018). <https://doi.org/10.1016/j.est.2018.03.012>
- K.K. Sadasivuni, D. Ponnamma, J. Kim, J.J. Cabibihan, M.A. Almaadeed, *Composites in Super Capacitor* (Elsevier Inc., Amsterdam, 2017). <https://doi.org/10.1016/B978-0-12-809261-3/00018-8>
- Y. Wang, Y. Song, Y. Xia, Electrochemical capacitors: mechanism, materials, systems, characterization and applications. *Chem. Soc. Rev.* **45**, 5925–5950 (2016). <https://doi.org/10.1039/c5cs00580a>
- S. Khamlich, Z. Abdullaeva, J.V. Kennedy, M. Maaza, High performance symmetric supercapacitor based on zinc hydroxychloride nanosheets and 3D graphene-nickel foam composite. *Appl. Surf. Sci.* **405**, 329–336 (2017). <https://doi.org/10.1016/j.apsusc.2017.02.095>
- K. Kaviyarasu, E. Manikandan, J. Kennedy, M. Jayachandran, R. Ladchumananandasivam, U.U. De Gomes, M. Maaza, Synthesis and characterization studies of NiO nanorods for enhancing solar cell efficiency using photon upconversion materials. *Ceram. Int.* **42**, 8385–8394 (2016). <https://doi.org/10.1016/j.ceramint.2016.02.054>
- Q. Jiang, N. Kurra, M. Alhabeab, Y. Gogotsi, H.N. Alshareef, All pseudocapacitive MXene-RuO₂ asymmetric supercapacitors. *Adv. Energy Mater.* **8**, 1–10 (2018). <https://doi.org/10.1002/aenm.201703043>
- C. Wu, Y. Xu, L. Ao, K. Jiang, L. Shang, Y. Li, Z. Hu, J. Chu, Robust three-dimensional porous rGO aerogel anchored with ultra-fine α -Fe₂O₃ nanoparticles exhibit dominated pseudocapacitance behavior for superior lithium storage. *J. Alloys Compd.* **816**, 152627 (2020). <https://doi.org/10.1016/j.jallcom.2019.152627>
- V. Velmurugan, U. Srinivasarao, R. Ramachandran, M. Saranya, A.N. Grace, Synthesis of tin oxide/graphene (SnO₂/G) nanocomposite and its electrochemical properties for supercapacitor applications. *Mater. Res. Bull.* **84**, 145–151 (2016). <https://doi.org/10.1016/j.materresbull.2016.07.015>
- X. Yang, C. Cai, Y. Zou, C. Xiang, H. Chu, E. Yan, S. Qiu, L. Sun, F. Xu, X. Hu, Co₃O₄-doped two-dimensional carbon nanosheet as an electrode material for high-performance asymmetric supercapacitors. *Electrochim. Acta* **335**, 135611 (2020). <https://doi.org/10.1016/j.electacta.2020.135611>
- N. Duraisamy, A. Numan, S.O. Fatin, K. Ramesh, S. Ramesh, Facile sonochemical synthesis of nanostructured NiO with different particle sizes and its electrochemical properties for supercapacitor application. *J. Colloid Interface Sci.* **471**, 136–144 (2016). <https://doi.org/10.1016/j.jcis.2016.03.013>
- X. Wu, F. Yang, H. Dong, J. Sui, Q. Zhang, J. Yu, Q. Zhang, L. Dong, Controllable synthesis of MnO₂ with different structures for supercapacitor electrodes. *J. Electroanal. Chem.* **848**, 113332 (2019). <https://doi.org/10.1016/j.jelechem.2019.113332>
- S. Shivakumara, T.R. Penki, N. Munichandraiah, High specific surface area α -Fe₂O₃ nanostructures as high performance electrode material for supercapacitors. *Mater. Lett.* **131**, 100–103 (2014). <https://doi.org/10.1016/j.matlet.2014.05.160>
- Y. Zeng, M. Yu, Y. Meng, P. Fang, X. Lu, Y. Tong, Iron-based supercapacitor electrodes: advances and challenges. *Adv. Energy Mater.* **6**, 1–17 (2016). <https://doi.org/10.1002/aenm.201601053>
- A.K. Mishra, J. At, Concepts and applications. *Mol. Condens. Nano Phys.* **5**, 159–193 (2018). <https://doi.org/10.26713/jamcnp.v5i2.842>
- H. Zhou, G. Han, One-step fabrication of heterogeneous conducting polymers-coated graphene oxide/carbon

- nanotubes composite films for high-performance supercapacitors. *Electrochim. Acta* **192**, 448–455 (2016). <https://doi.org/10.1016/j.electacta.2016.02.015>
16. B. Saravanakumar, G. Ravi, V. Ganesh, S. Ravichandran, A. Sakunthala, R. Yuvakkumar, Low surface energy and pH Effect on SnO₂ nanoparticles formation for supercapacitor applications. *J. Nanosci. Nanotechnol.* **19**, 3429–3436 (2019). <https://doi.org/10.1166/jnn.2019.16098>
 17. P. Liu, Y. Zhu, X. Gao, Y. Huang, Y. Wang, S. Qin, Y. Zhang, Rational construction of bowl-like MnO₂ nanosheets with excellent electrochemical performance for supercapacitor electrodes. *Chem. Eng. J.* **350**, 79–88 (2018). <https://doi.org/10.1016/j.cej.2018.05.169>
 18. Y. Hu, C. Guan, Q. Ke, Z.F. Yow, C. Cheng, J. Wang, Hybrid Fe₂O₃ Nanoparticle Clusters/rGO Paper as an Effective Negative Electrode for Flexible Supercapacitors. *Chem. Mater.* **28**, 7296–7303 (2016). <https://doi.org/10.1021/acs.cemmater.6b02585>
 19. K.P. Gannavarapu, R.B. Dandamudi, Shape engineered three dimensional α -Fe₂O₃-activated carbon nano composite as enhanced electrochemical supercapacitor electrode material. *Int. J. Energy Res.* **42**, 4687–4696 (2018). <https://doi.org/10.1002/er.4211>
 20. Z. Yang, L. Tang, J. Ye, D. Shi, S. Liu, M. Chen, Hierarchical nanostructured α -Fe₂O₃/polyaniline anodes for high performance supercapacitors. *Electrochim. Acta* **269**, 21–29 (2018). <https://doi.org/10.1016/j.electacta.2018.02.144>
 21. Z.-G. Yang, N.-N. Liu, S. Dong, F.-S. Tian, Y.-P. Gao, Z.-Q. Hou, Supercapacitors based on free-standing reduced graphene oxides/carbon nanotubes hybrid films. *SN Appl. Sci.* **1**, 1–9 (2019). <https://doi.org/10.1007/s42452-018-0059-y>
 22. S.N. Khatavkar, S.D. Sartale, α -Fe₂O₃ thin film on stainless steel mesh: a flexible electrode for supercapacitor. *Mater. Chem. Phys.* **225**, 284–291 (2019). <https://doi.org/10.1016/j.matchemphys.2018.12.079>
 23. A.M. Díez-pascual, C. Sainz-urruela, C. Vallés, S. Vera-lópez, M.P.S. Andrés, Tailorable synthesis of highly oxidized graphene oxides via an environmentally-friendly electrochemical process. *Nanomaterials* **10**, 1–18 (2020). <https://doi.org/10.3390/nano10020239>
 24. C. Zhao, X. Shao, Y. Zhang, X. Qian, Fe₂O₃/RGO/Fe₃O₄ composite in-situ grown on Fe foil for high performance supercapacitors. *ACS Appl. Mater. Interfaces* **8**(44), 30133–30142 (2016)
 25. N. Cao, Y. Zhang, Study of reduced graphene oxide preparation by Hummers' method and related characterization. *J. Nanomater.* (2015). <https://doi.org/10.1155/2015/168125>
 26. N.I. Zaaba, K.L. Foo, U. Hashim, S.J. Tan, W.W. Liu, C.H. Voon, Synthesis of graphene oxide using modified Hummers method: solvent influence. *Procedia Eng.* **184**, 469–477 (2017). <https://doi.org/10.1016/j.proeng.2017.04.118>
 27. Y. Wang, H. Zhang, R. Hu, J. Liu, T. van Ree, H. Wang, L. Yang, M. Zhu, Fe₃O₄/SnO₂/rGO ternary composite as a high-performance anode material for lithium-ion batteries. *J. Alloys Compd.* **693**, 1174–1179 (2017). <https://doi.org/10.1016/j.jallcom.2016.10.082>
 28. B. Saravanakumar, C. Radhakrishnan, M. Ramasamy, R. Kaliaperumal, A.J. Britten, M. Mkandawire, Copper oxide/mesoporous carbon nanocomposite synthesis, morphology and electrochemical properties for gel polymer-based asymmetric supercapacitors. *J. Electroanal. Chem.* **852**, 113504 (2019). <https://doi.org/10.1016/j.jelechem.2019.113504>
 29. X. Pan, X. Chen, Y. Li, Z. Yu, Facile synthesis of Co₃O₄ nanosheets electrode with ultrahigh specific capacitance for electrochemical supercapacitors. *Electrochim. Acta* **182**, 1101–1106 (2015). <https://doi.org/10.1016/j.electacta.2015.10.035>
 30. M. Jana, P. Sivakumar, M. Kota, M.G. Jung, H.S. Park, Phase- and interlayer spacing-controlled cobalt hydroxides for high performance asymmetric supercapacitor applications. *J. Power Sources* **422**, 9–17 (2019). <https://doi.org/10.1016/j.jpowsour.2019.03.019>
 31. H. Wang, H. Yi, X. Chen, X. Wang, Asymmetric supercapacitors based on nano-architected nickel oxide/graphene foam and hierarchical porous nitrogen-doped carbon nanotubes with ultrahigh-rate performance. *J. Mater. Chem. A* **2**, 3223–3230 (2014). <https://doi.org/10.1039/c3ta15046a>
 32. J. Ding, S. Zhu, T. Zhu, W. Sun, Q. Li, G. Wei, Z. Su, Hydrothermal synthesis of zinc oxide-reduced graphene oxide nanocomposites for an electrochemical hydrazine sensor. *RSC Adv.* **5**, 22935–22942 (2015). <https://doi.org/10.1039/c5ra00884k>
 33. N. Duraisamy, K. Kandiah, R. Rajendran, S. Prabhu, R. Ramesh, G. Dhanaraj, Electrochemical and photocatalytic investigation of nickel oxide for energy storage and wastewater treatment. *Res. Chem. Intermed.* **44**, 5653–5667 (2018). <https://doi.org/10.1007/s11164-018-3446-5>
 34. N. Thangavel, S. Bellamkonda, A.D. Arulraj, G. Ranga Rao, B. Neppolian, Visiblelight induced efficient hydrogen production through semiconductor-conductor-semiconductor (S-C-S) interfaces formed between g-C₃N₄ and rGO/Fe₂O₃ core-shell composites. *Catal. Sci. Technol.* **8**, 5081–5090 (2018). <https://doi.org/10.1039/c8cy01248b>
 35. S.M. Botsa, G.P. Naidu, M. Ravichandra, S.J. Rani, R.B. Anjaneyulu, C.V. Ramana, Flowerlike SnO₂-Fe₂O₃-rGO ternary composite as highly efficient visible light induced photocatalyst for the degradation of organic pollutants from contaminated water. *J. Mater. Res. Technol.* **9**, 12461–12472 (2020). <https://doi.org/10.1016/j.jmrt.2020.08.087>

36. S. Wang, F. Ma, H. Jiang, Y. Shao, Y. Wu, X. Hao, Band gap-tunable porous borocarbonitride nanosheets for high energy-density supercapacitors. *ACS Appl. Mater. Interfaces*. **10**, 19588–19597 (2018). <https://doi.org/10.1021/acsami.8b02317>
37. A. Ali, H. Zafar, M. Zia, I. ul Haq, A.R. Phull, J.S. Ali, A. Hussain, Synthesis, characterization, applications, and challenges of iron oxide nanoparticles. *Nanotechnol. Sci. Appl.* **9**, 49–67 (2016). <https://doi.org/10.2147/NSA.S99986>
38. R. Barik, M. Mohapatra, Solvent mediated surface engineering of α -Fe₂O₃ nanomaterials: Facet sensitive energy storage materials. *CrystEngComm* **17**, 9203–9215 (2015). <https://doi.org/10.1039/c5ce01369k>
39. Q. Zhang, P. Liu, C. Miao, Z. Chen, C.M. Lawrence Wu, C.H. Shek, Formation of orthorhombic SnO₂ originated from lattice distortion by Mn-doped tetragonal SnO₂. *RSC Adv.* **5**, 39285–39290 (2015). <https://doi.org/10.1039/c5ra04946f>
40. T. Wang, Y. Li, L. Wang, C. Liu, S. Geng, X. Jia, F. Yang, L. Zhang, L. Liu, B. You, X. Ren, H. Yang, Synthesis of graphene/ α -Fe₂O₃ composites with excellent electromagnetic wave absorption properties. *RSC Adv.* **5**, 60114–60120 (2015). <https://doi.org/10.1039/c5ra09715k>
41. K. Wongsaprom, R.A. Bornphotsawatkun, E. Swatsitang, Synthesis and characterization of tin oxide (SnO₂) nanocrystalline powders by a simple modified sol–gel route. *Appl. Phys. A Mater. Sci. Process.* **114**, 373–379 (2014). <https://doi.org/10.1007/s00339-013-8197-y>
42. B.A. Aragaw, Reduced graphene oxide-intercalated graphene oxide nano-hybrid for enhanced photoelectrochemical water reduction. *J. Nanostruct. Chem.* **10**, 9–18 (2020). <https://doi.org/10.1007/s40097-019-00324-x>
43. D.L.A. de Faria, S. Venâncio Silva, M.T. de Oliveira, Raman microspectroscopy of some iron oxides and oxyhydroxides. *J. Raman Spectrosc.* **28**, 873–878 (1997). [https://doi.org/10.1002/\(sici\)1097-4555\(199711\)28:11<873::aid-jrs177>3.3.co;2-2](https://doi.org/10.1002/(sici)1097-4555(199711)28:11<873::aid-jrs177>3.3.co;2-2)
44. J. Kennedy, F. Fang, J. Futter, J. Leveneur, P.P. Murmu, G.N. Panin, T.W. Kang, E. Manikandan, Synthesis and enhanced field emission of zinc oxide incorporated carbon nanotubes. *Diam. Relat. Mater.* **71**, 79–84 (2017). <https://doi.org/10.1016/j.diamond.2016.12.007>
45. E. Manikandan, G. Kavitha, J. Kennedy, Epitaxial zinc oxide, graphene oxide composite thin-films by laser technique for micro-Raman and enhanced field emission study. *Ceram. Int.* **40**, 16065–16070 (2014). <https://doi.org/10.1016/j.ceramint.2014.07.129>
46. S. Wang, Y. Dong, C. He, Y. Gao, N. Jia, Z. Chen, W. Song, The role of sp²/sp³ hybrid carbon regulation in the nonlinear optical properties of graphene oxide materials. *RSC Adv.* **7**, 53643–53652 (2017). <https://doi.org/10.1039/c7ra10505c>
47. M. Zhang, D. Lei, Z. Du, X. Yin, L. Chen, Q. Li, Y. Wang, T. Wang, Fast synthesis of SnO₂/graphene composites by reducing graphene oxide with stannous ions. *J. Mater. Chem.* **21**, 1673–1676 (2011). <https://doi.org/10.1039/c0jm03410j>
48. I.J. Gomez, B. Arnaiz, M. Cacioppo, F. Arcudi, M. Prato, Nanocrystalline Fe-Fe₂O₃ particle-deposited N-doped graphene as an activity modulated Pt-free electrocatalyst for oxygen reduction reaction. *J. Mater. Chem. B.* (2018). <https://doi.org/10.1039/x0xx00000x>
49. A. Manuscript, CrystEngComm, (n.d.)
50. M.G.T.N. D., J.M.B.S.P. Basu, R. Mahesh, S. Harish, S. Joseph, P. Sagayaraj, One-pot hydrothermal preparation of Cu₂O-CuO/rGO nanocomposites with enhanced electrochemical performance for supercapacitor applications. *Appl. Surf. Sci.* **449**, 474–484 (2018). <https://doi.org/10.1016/j.apsusc.2017.12.199>
51. Z. Shen, H. Xing, Y. Zhu, X. Ji, Z. Liu, L. Wang, Synthesis and enhanced microwave-absorbing properties of SnO₂/ α -Fe₂O₃@rGO composites. *J. Mater. Sci. Mater. Electron.* **28**, 13896–13904 (2017). <https://doi.org/10.1007/s10854-017-7238-2>
52. F. Paquin, J. Rivnay, A. Salleo, N. Stingelin, C. Silva, Multi-phase semicrystalline microstructures drive exciton dissociation in neat plastic semiconductors. *J. Mater. Chem. C.* **3**, 10715–10722 (2015). <https://doi.org/10.1039/b000000x>
53. G. Zhao, T. Wen, C. Chen, X. Wang, Synthesis of graphene-based nanomaterials and their application in energy-related and environmental-related areas. *RSC Adv.* **2**, 9286–9303 (2012). <https://doi.org/10.1039/c2ra20990j>
54. W.P.S.L. Wijesinghe, M.M.M.G.P.G. Mantilaka, K.A.A. Ruparathna, R.B.S.D. Rajapakshe, S.A.L. Sameera, M.G.G.S.N. Thilakarathna, *Filler Matrix Interfaces of Inorganic/Biopolymer Composites and Their Applications* (Elsevier Ltd, Amsterdam, 2019). <https://doi.org/10.1016/B978-0-08-102665-6.00004-2>
55. G. Xia, N. Li, D. Li, R. Liu, C. Wang, Q. Li, X. Lü, J.S. Spendelov, J. Zhang, G. Wu, Graphene/Fe₂O₃/SnO₂ ternary nanocomposites as a high-performance anode for lithium ion batteries. *ACS Appl. Mater. Interfaces.* **5**, 8607–8614 (2013). <https://doi.org/10.1021/am402124r>
56. T. Li, A. Qin, L. Yang, J. Chen, Q. Wang, D. Zhang, H. Yang, In situ grown Fe₂O₃ single crystallites on reduced graphene oxide nanosheets as high performance conversion anode for sodium-ion batteries. *ACS Appl. Mater. Interfaces.* **9**, 19900–19907 (2017). <https://doi.org/10.1021/acsami.7b04407>
57. L. Chen, D. Liu, P. Yang, Preparation of α -Fe₂O₃/rGO composites toward supercapacitor applications. *RSC Adv.* **9**, 12793–12800 (2019). <https://doi.org/10.1039/c9ra01928f>

58. W. Peng, G. Han, Y. Huang, Y. Cao, S. Song, Insight the effect of crystallinity of natural graphite on the electrochemical performance of reduced graphene oxide. *Results Phys.* **11**, 131–137 (2018). <https://doi.org/10.1016/j.rinp.2018.08.055>
59. M.T.T. Tran, B. Tribollet, V. Vivier, M.E. Orazem, On the impedance response of reactions influenced by mass transfer. *Russ. J. Electrochem.* **53**, 932–940 (2017). <https://doi.org/10.1134/S1023193517090142>
60. E. Samuel, T.G. Kim, C.W. Park, B. Joshi, M.T. Swihart, S.S. Yoon, Supersonically sprayed $Zn_2SnO_4/SnO_2/CNT$ nanocomposites for high-performance supercapacitor electrodes. *ACS Sustain. Chem. Eng.* **7**, 14031–14040 (2019). <https://doi.org/10.1021/acssuschemeng.9b02549>

Publisher's Note Springer Nature remains neutral with regard to jurisdictional claims in published maps and institutional affiliations.